Seismogram Analysis and Fitting of South Sumatra Earthquakes in CHTO, QIZ, KMI, ENH, and SSE Observatory Stations

Bagus Jaya Santosa

Lecturer, Geophysics Dept., FMIPA, ITS, Jl. Arif Rahman Hakim 1, Surabaya 60111, Indonesia, email: bjs@physics.its.ac.id

ABSTRACT

This research investigated the S wave velocity structure below SE Asia, by analyzing the seismograms of South Sumatra earthquakes at CHTO, QIZ, KMI, ENH and SSE stations, in the time domain and three Cartesian components simultaneously. The main data is waveform comparison between the measured seismogram and synthetic one, instead of travel time or indirect data from dispersion curve, as other seismological researches. The synthetic seismogram constructed from anisotropic PREM global earth model deviates greatly from the measured one, from surface wave to multiple core reflected waves. Corrections cover the gradient change of β_h in the upper mantle layers, which turns from negative into positive, as stated in the anisotropic PREM, changes of earth crust depth and zero order coefficients of β velocity function in all earth mantle layers. So the fitting is obtained on the arrival time, the Love and Rayleigh surface wave, the S, and the repetitive core reflected ScS, ScS_2 and ScS_3 waves. This result reveals that South East Asia, being stretched due to tectonic release, has a mantle part with negative anomaly on S wave velocity and vertical anisotropy in all earth mantle layers. Error in CMT solution is shown by distinct amplitude differences in the surface waves.

Keywords:
Seismogram analysis;
Vertical anisotropy;
Negative Anomaly;
Non-active seismic zone;
Error in CMT solution

1. Introduction

During the last two decades, with the exploitation of computer capacity and the improvement of seismic data quality, seismologists have opened a new field of study on seismogram, and have applied the new technology to map the 3 dimensions earth structure [1-4]. Although new technology has been exploited, the data set used is still the travel time data of body wave phases and the indirect data from the dispersion curve on the surface wave [5]. These studies have greatly developed our understanding about the earth structure and dynamics of the earth interior.

The seismology procedure for quantitative analysis on the seismogram is generally the arrival time measurement of main wave phases, and the dispersion relation calculation of the surface wave. *P* wave arrival time is the easiest wave to be measured due to the first break. Using the *P* wave arrival time data and by applying the inversion theory, the earthquake parameter and the earth structure can be obtained. The

two main quantitative methods above were used to analyze the seismogram evaluation only at some certain points in a seismogram time series.

The structure of the *P* wave velocity in the same region as previous research of the seismograms [1, 6, 7, 8] is obtained by directly inverting the *P* travel time data, in which the numbers reach circa 8×10^6, the phase of the reflected wave *pP* circa 0.6×10^6, and phase biased into the earth core *PcP*, circa 1×10^6. These data are collected from 300,000 earthquakes from time range of 1/1/1964 to 31/12/2000. Similarly, a small number of data consisting of the differential travel time *PP-P*, *PKP-P$_{diff}$* which are measured accurately by waveform cross-correlation from broad band digital data.

The objective of this research is to analyze the seismogram data of earthquakes in south Sumatra, that lie close to each other, recorded at *CHTO*, Thailand, *QIZ*, *KMI*, *ENH* and *SSE* stations, China. The wave

paths from the earthquake hypocenters to observatory stations pass across the non tectonic structure beneath *SE* Asia. The method used is different to other seismological method, in which the evaluated data only analyze little information in the seismogram time series to interpret the earth structure. Although the data set used by other seismologists includes millions of travel time, it only contains little information in the seismogram time series. In contrast, the waveform of the *S* wave, the Love and Rayleigh surface waves in three Cartesian components simultaneously, and the core reflected waves *ScS* and repetitive *ScS*$_2$, carry all information of the seismogram.

2. Theory

The following consideration will be written down shortly for an equation system of ground movement as an effect of wave propagation that is excited by an earthquake.

These systems represent the mathematical method for the *GEMINI* [9-10] program, where the calculation of synthetic seismogram is conducted by solving the equation systems in complex frequency domain.

In general ground movement is a differential equation systems in time domain, which its derivative to time disappear when transformed to frequency domain as shown in Eq. (1)

$$\rho\omega^2 u = \nabla.\sigma + f \tag{1}$$

Because the earth is depicted as a ball, the coordinate system used is spherical coordinate. Strain, divergence of tension and force are expressed as, in Eq. (2):

$$u = U e_r + \nabla_1 V - e_r \times \nabla_1 W$$
$$\sigma = R e_r + \nabla_1 S - e_r \times \nabla_1 T \tag{2}$$
$$f = K e_r + \nabla_1 H - e_r \times \nabla_1 K$$

where *U*, *V* and *W* are components of ground movement in vertical, east-west and north-south direction. Earthquake source is supposed to be located in North Pole, also decomposition for divergence tension (*R*, *S* and *T*) and force vector (*G*, *H* and *K*), and the surface gradient is shown in Eq. (3).

$$\nabla_1^2 = \frac{\partial^2}{\partial\vartheta^2} + \frac{1}{\sin^2\vartheta}\frac{\partial^2}{\partial\varphi^2} + \cot\vartheta\frac{\partial}{\partial\vartheta} \tag{3}$$

$\hat{\vartheta}$ and $\hat{\varphi}$ are unit vectors in the direction of ϑ and φ.

Hooke's law describes the relation between strain, force and tension. Using the expansion of spherical harmonic function this relation can be written down as, see Eq. (4).

$$U(r,\vartheta,\varphi,\omega) = \sum_{l=0}^{\infty} U_l^m(r,\omega) Y_l^m(\vartheta,\varphi) \tag{4}$$

where *U* is spherical harmonic coefficient. The wave equation becomes six coupled first order differential equations system, see Eq. (5).

$$\frac{d}{dr}y(r) = A.y(r) + z(r) \tag{5}$$

The first three components of *y* vector are the ground movement in the spherical coordinates, and the next three ones are for tension, see Eq (6).

Form of the differential equation system for the spheroidal movement is in the form of 4x4 system, i.e.:

$$d\hat{U}_l^m = \frac{1}{\tilde{C}}\left[\tilde{R}_l^m - \frac{\tilde{F}}{r}\left(2\tilde{U}_l^m - l(l+1)\tilde{V}_l^m\right)\right]$$

$$\frac{d\tilde{R}_l^m}{dr} = -\rho_0\omega^2\tilde{U}_l^m + \frac{2}{r}\left(\tilde{F}\frac{d\tilde{U}_l^m}{dr} - \tilde{R}_l^m\right) + \frac{l(l+1)}{r}\tilde{S}_l^m$$
$$+ \frac{1}{r}\left[\frac{2}{r}\left(\tilde{A}-\tilde{N}\right) - \rho_0 g_0\right]\left(2\tilde{U}_l^m - l(l+1)\tilde{V}_l^m\right)$$
$$- \rho_0\left(\frac{l+1}{r}\tilde{\phi}_l^m - \tilde{Q}_l^m + \frac{2g_0}{r}\tilde{U}_l^m\right) - \tilde{G}_l^m$$

$$\frac{d\tilde{V}_l^m}{dr} = \frac{1}{\tilde{L}}\tilde{S}_l^m + \frac{1}{r}\left(\tilde{V}_l^m - \tilde{U}_l^m\right) \tag{6}$$

$$\frac{d\tilde{S}_l^m}{dr} = -\rho_0\omega^2\tilde{V}_l^m - \frac{\tilde{F}}{r}\frac{d\tilde{U}_l^m}{dr} + \frac{\tilde{A}}{dr}\left(2\tilde{U}_l^m - l(l+1)\tilde{V}_l^m\right)$$
$$+ \frac{2\tilde{N}}{r^2}\left(\tilde{U}_l^m - \tilde{V}_l^m\right) - \frac{3}{r}\tilde{S}_l^m + \frac{\rho_0}{r}\left(\tilde{\phi}_l^m + g_0\tilde{U}_l^m\right) - \tilde{H}_l^m$$

$$\frac{d\tilde{\phi}_l^m}{dr} = \tilde{Q}_l^m - 4\pi\gamma\rho_0\tilde{U}_l^m - \frac{l+1}{r}\tilde{\phi}_l^m$$

$$\frac{d\tilde{Q}_l^m}{dr} = \frac{l-1}{r}\left(\tilde{Q}_l^m - 4\pi\gamma\rho_0\tilde{U}_l^m\right) - \frac{4\pi\gamma\rho_0}{r}\left(2\tilde{U}_l^m - l(l+1)\tilde{V}_l^m\right)$$

and system of 2×2 for toroidal movement as shown in Eq. (7).

$$\frac{d\tilde{W}_l^m}{dr} = \frac{1}{\tilde{L}}\tilde{T}_l^m + \frac{1}{r}\tilde{W}_l^m$$

$$\frac{d\tilde{T}_l^m}{dr} = -\frac{3}{r}\tilde{T}_l^m - \left(\rho_0\omega^2 + \frac{\tilde{N}}{r^2}\left[2 - l(l+1)\right]\right)\tilde{W}_l^m - \tilde{K}_l^m \tag{7}$$

A, *F*, *C*, *L*, *N* and ρ are elastic parameters of earth's constitute rock. The laid over quantities tilde notation means that the independent variable is complex frequency. Here it can be seen that both elastic parameters *L* and *N* exist in equation of motion (*V* and *W*). Both these parameters give the major

effect at Love and Rayleigh wave. Expansion for spherical harmonic coefficient is also calculated for terms in tensor moment of the earthquake, which forces can be expressed as stress divergence, see Eq. (8).

$$f = \nabla . m \qquad (8)$$

where m is symmetry and disappears at the earth surface.

So the expansion of spherical harmonic for forces contains coefficients with the δ function (index 1) and its first derivation to r (index 2), see Eq. (9).

$$z(r) = z_1 \delta(r - r_s) + z_2 \frac{d}{dr} \delta(r - r_s) \qquad (9)$$

Because the forces has been expanded also in spherical harmonic functions, thereafter the expanded forces are reinserted into wave equation and its result is in the form of order one differential equation system. In such equation as this, the parameters of solid elastic substance enter at the components of kernel matrix.

To include the nature of inelastic earth, the real frequency ω is changed to complex frequency by introducing a small positive imaginer number, notated by σ, becoming $\omega + i\sigma$. This differential systems is integrated, one from the middle point of earth core, or from a radius point, where the amplitude of a wave phase in that point has exponentially decayed, until the earthquake source depth (notated by g_1 and g_2, others by integration from the earth surface to the source depth (w_1 and w_2). The solution must fulfill the boundary condition at earth surface in which the tension is equal to zero, and also at the interface of solid and fluid, that the shear tension should disappear. Result of integration, the so-called Green's function is later tapered down and the results are then compared to the coefficient of expanded source, see Eq. (10).

$$s = y(r_s + 0) - y(r_s - 0)$$
$$= z_1 + A(r_s) \qquad (10)$$

where r_s is the earthquake source depth, and s is the earthquake strength whose components are the elements of the *CMT* solution, shown in Eq. (11).

$$c_1 g_1(r_s) + c_2 g_2(r_s) - d_1 w(r_s) - d_2 w_2(r_s) = s(r_s) \qquad (11)$$

Each amplitude function of spheroidal and toroidal movement is solved using the Cramer's rule.

The solution of linear equation with the Cramer's rule needs the existence of discriminator formed by Green's function multiplication values at source depth has finite values. But at eigen frequencies the

discriminator has zero value. Because the weakness of numeric systems, values of Green's functions integration have big order, but the difference between Green's functions multiplication has small values which is smaller than the numerically 'round-off'.

To overcome this difficulty, the differential equation systems are altered into differential minors calculation form. With help of matrix coefficients from the homogen systems, the differential equation system for the minors was formulated in Eqs. (12) and (13):

$$\frac{dm_2}{dr} = -\frac{2}{r} m_1 - \frac{2l(l+1)}{r^2} \left(\tilde{A} - \frac{\tilde{F}^2}{\tilde{C}} - \tilde{N} \right) m_2 + \frac{l(l+1)}{r} m_3$$
$$- \frac{l(l+1)\tilde{F}}{r\tilde{C}} m_4$$

$$\frac{dm_2}{dr} = \frac{1}{r} \left(1 - \frac{2\tilde{F}}{\tilde{C}} \right) m_2 + \frac{1}{\tilde{L}} m_3 + \frac{1}{\tilde{C}} m_4$$

$$\frac{dm_3}{dr} = -\frac{2\tilde{F}}{r\tilde{C}} m_1 + \left[-\omega^2 \rho_0 + \frac{l(l+1)}{r^2} \left(\tilde{A} - \frac{\tilde{F}^2}{\tilde{C}} \right) - \frac{2\tilde{N}}{r^2} \right] m_2$$
$$- \frac{1}{r} \left(3 + \frac{2\tilde{F}}{\tilde{C}} \right) m_3 + \frac{1}{\tilde{C}} m_5 \quad 12)$$

$$\frac{dm_4}{dr} = \frac{2}{r} m_1 + \left[-\omega^2 \rho_0 + \frac{4}{r^2} \left(\tilde{A} - \frac{\tilde{F}^2}{\tilde{C}} - \tilde{N} \right) \right] m_2 \qquad (12)$$
$$- \frac{1}{r} \left(1 - \frac{2\tilde{F}}{\tilde{C}} \right) m_4 + \frac{1}{\tilde{L}} m_5$$

$$\frac{dm_5}{dr} = \frac{4}{r^2} \left(\tilde{A} - \frac{\tilde{F}^2}{\tilde{C}} - \tilde{N} \right) m_1$$
$$+ \left[-\omega^2 \rho_0 + \frac{4}{r^2} \left(\tilde{A} - \frac{\tilde{F}^2}{\tilde{C}} - \tilde{N} \right) \right] m_3$$
$$+ \left[-\omega^2 \rho_0 + \frac{l(l+1)}{r^2} \left(\tilde{A} - \frac{\tilde{F}^2}{\tilde{C}} \right) - \frac{2\tilde{N}}{r^2} \right] m_4$$
$$+ \frac{1}{r} \left(\frac{2\tilde{F}}{\tilde{C}} - 5 \right) m_5$$

and

$$m_6 = -\frac{1}{l(l+1)} m_1 \qquad (13)$$

The last equation must be fulfilled by the equation system integration. This differential minors system is later finished with ordinary integration method. Complete description for theory of wave propagation in the earth medium can be found at article from Dalkolmo [9].

Hence, Green's function amplitude is still in complex frequency. It can be finished for an earth

model with complete parameter elastic, source depth and strength of earthquake. To obtain the synthetic seismogram at an observation station, the station's epicentral distance and azimuth from the earthquake source are given, and from these parameters the spherical harmonic functions are expanded. When the minors are completely calculated, the spherical harmonic functions are summed for that station's coordinate. The results are afterwards back Fourier transformed to the time domain.

The synthetic seismogram is calculated using *GEMINI* Program, which is equivalent with the Summation of Normal Mode method, but the difference is in the independent variable used. The *GEMINI* uses the complex frequency, instead of real frequency as in the Summation of Normal Mode.

3. Data and Method

Before analyzing the seismogram, we should be able to identify the wave phases in the seismogram. A calculation program of the synthetic travel time of main body phases is needed to run, i.e. *TTIMES* program based on a paper by Bulland and Chapman [11], obtained from http://orfeus-eu.org. The data set used give a seismogram comparison between the measured seismogram and the synthetic one. The synthetic seismogram is calculated by the *GEMINI* method (Green function of the Earth by *MINor* Integration). The *GEMINI* program calculates the minors of Green functions for a given earth model (initially the anisotropic *PREM* [12], hereafter *PREMAN*), and for a certain depth of the earthquake source. The other global earth model, such as *IASPEI*91 [13] and *AK*135 [14] are not used in this research as an initial model, because seismogram comparison on Love and Rayleigh surface waves shows that the anisotropy factor in the earth model should be taken out.

This research analyzes the seismograms which were generated by earthquakes in Southern Sumatra, whereas the data were recorded in *CHTO*, *QIZ*, *KMI*, *ENH* and *SSE* observatory stations, to understand the *S* wave velocity structure beneath *SE* Asia. Table (1) presents the three-dimensional location of the analyzed earthquakes. It indicates that these four earthquakes hypocenter lie very close to each other.

Figure (1) shows the vertical projection of the wave paths from the earthquake sources in South Sumatra to the *CHTO*, *QIZ*, *KMI*, *ENH,* and *SSE* stations. The wave paths pass across the northern side of Southeast Asian that lies on the front side of Indian subduction zone.

Table 1. The position of the earthquake sources according to the global Centroid Moment-Tensor catalog.

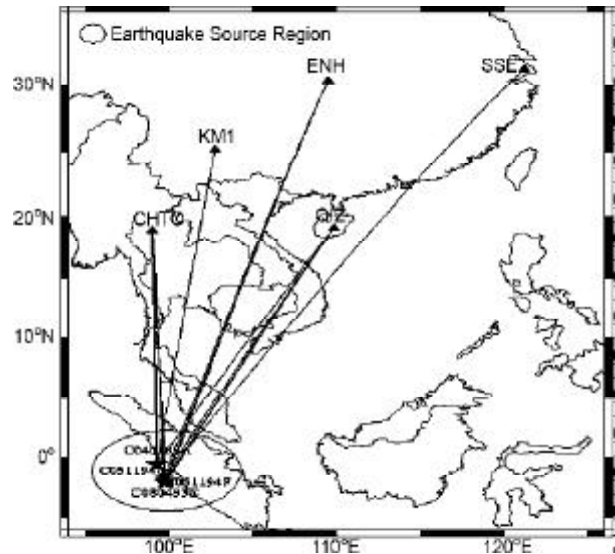| No	Earthquake Datum & Time, Code	°Latitude	°Longitude	Depth (km)	Mw (SR)
1	110594, 21:14:34.0 B051194F	-2.06	99.72	15.0	5.8
2	110594, 08:18:16.9 C051194C	-2.00	99.80	15.0	6.3
3	010498, 17:56:23.4 C040198A	-0.54	99.26	41.9	6.9
4	040893, 11:31:18.1 C080493C	-1.62	99.68	17.0	6.4

Figure 1. The vertical projection of the wave paths from the earthquakes hypocenters to the CHTO, QIZ, KMI, ENH, and SSE observatory stations.

4. Seismogram Analysis and Discussion

4.1. Seismogram Analysis and Fitting

First, we analyze the seismogram of *B*051194*F* earthquake which occurred on May 11th 1994, recorded in *QIZ* station. The following figures present the seismogram comparison and fitting on the Love, Rayleigh, and *S*, and *ScS* waves. Figure contains 3 curves, where the solid curve is the measured data, the dotted curve is the synthetic seismogram constructed from the anisotropic *PREMAN* earth model, and the dot-dashed curve is the seismogram from the corrected earth model. The corrections of the *S* velocity structure cover the β_h velocity gradient in the upper mantle layers and the zero order coefficients of polynomial representing the β velocity structure in the earth mantle layers. The correction is needed to obtain seismogram fitting for *S* wave phase and the repetitive *S* waves, as well as the Love and Rayleigh surface wave. The correction result of the *S* velocity is displayed on a small box in the figure

on the right side as a dot-dashed curve, between the *PREMAN* and the corrected earth models.

Figure (2) presents seismogram analysis and fitting of the *B*051194*F* earthquake in *QIZ* station, beginning from the *S* wave phase to the Love and Rayleigh surface waves, and three figures on the same plate represent the seismogram pieces for core reflected wave *ScS*, *ScS$_2$* and *ScS$_3$* which pass all of the earth mantle layers from the earth surface down to *CMB* (Core Mantle Boundary), 2, 4 and 6 times respectively. It can be seen that the *PREMAN* earth model provides the synthetic seismogram, ranging from the Love and Rayleigh wave to the *S* body wave, with arrival times earlier than the measured

seismogram. Also, the great discrepancy on the Rayleigh wave in the *r* and *z* components could be seen. To solve these discrepancies, big negative correction on the *V* velocity structure in the lithosphere layers down to the depth 630*km* is required. Figures (2b), (2c) and (2d) present the seismogram pieces for *ScS*, *ScS$_2$* and *ScS$_3$* core reflected waves. Observation on these two depth waves, the synthetic from the *PREMAN* also provide little earlier arrival time. We notice the minima location of these waves, and to overcome the earlier travel time, the small negative correction values are also imposed to the β_v in the base mantle layers. The β_v velocity structure in the base mantle has bigger influence to *ScS* than the β_h
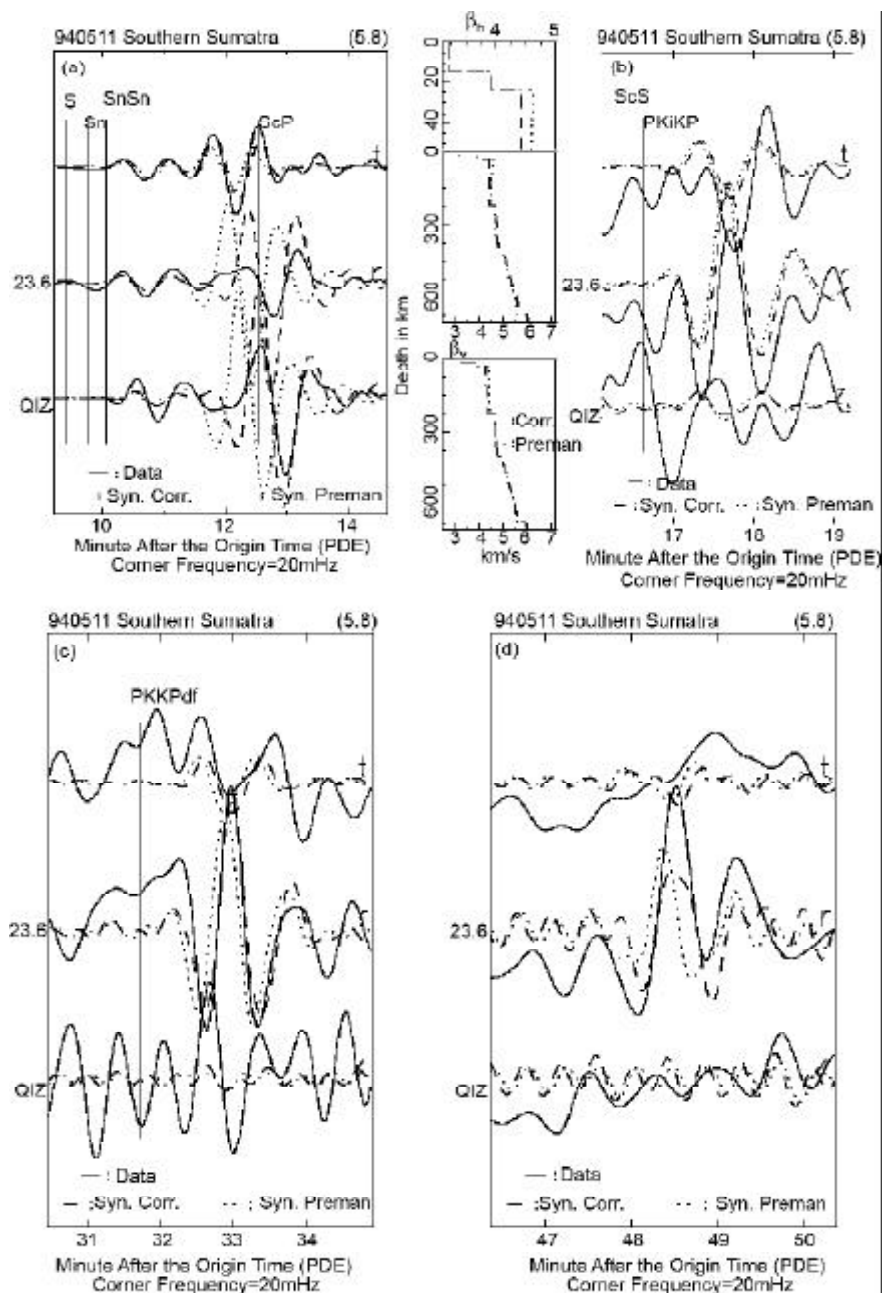

Figure 2. Seismogram analysis and fitting of B051194F earthquake in QIZ. waves: a) S-L-R; b) ScS; c) ScS$_2$; and d) ScS$_3$.

velocity structure. This factor is still not known by other seismologist. The travel time of *ScS* is circa 17 minute, so that the travel times of multiple *ScS*$_2$ and *ScS*$_3$ approximately around integer multiplication of *ScS* travel time. The *TTIMES* program does not provide the travel time of multiple core reflected *ScS* wave.

Next is the seismogram analysis of *B*051194*F* earthquake at *ENH* and *CHTO* observation stations as illustrated in Figures (3) and (4), respectively. The obtained earth model by seismogram analysis at *QIZ* is used to construct the synthetic seismogram at *ENH* and *CHTO* stations. It appears that the big negative

corrected earth model provides also seismogram fitting, which still needs small correction to obtain the seismogram fitting on Love and Rayleigh surface wave. This shows that the earth model beneath *SE* Asia has strong negative anomaly in the upper mantle layers and smaller negative anomaly on mantle layers down to *CMB*.

The seismogram analysis on the repetitive depth waves in a small epicentral distance stations (around 20º - 30º) opens a new way to investigate the velocity of S wave in the base mantle layers, as compared with the other seismologist using the time differences of *ScS-S*, or other wave phases, where the measurement
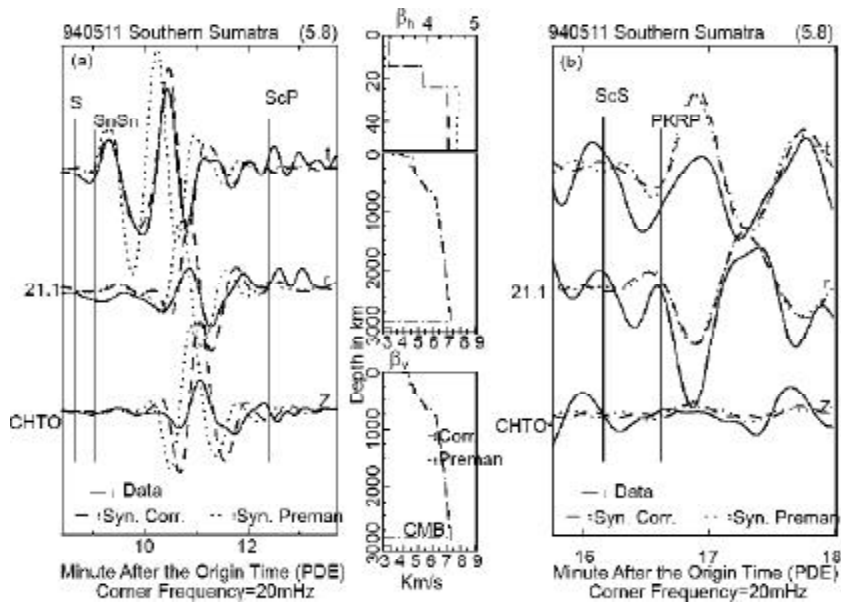

Figure 3. Seismogram analysis and fitting of B051194F earthquake in CHTO. waves: a) S-L-R; and b) ScS.
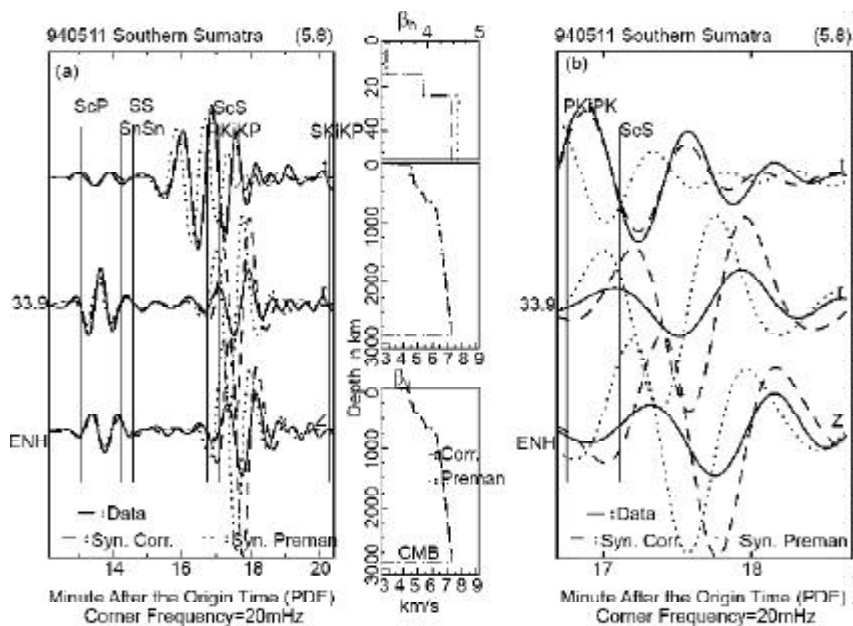

Figure 4. Seismogram analysis and fitting of B051194F earthquake in ENH. waves: a) S-L-R; and b) ScS.

can be taken just at an epicentral distance over 83° [15-16].

Figure (5) presents seismogram analysis and matching of *C051194C* earthquake in *QIZ* station. The second earthquake analysis, which has *B051194F* code, occur at the same day as the first one, and the earthquake sources are located very close to each other. An observation, ranges from *S* wave phase to the Love and Rayleigh surface wave in Figure (5a) and two figures in the right side for the seismogram pieces of *ScS* and ScS_2 depth wave. It can be seen that the synthetic seismogram constructed from *PREMAN* earth model provides all the wave phases with earlier arrival time than the measured one, and especially on the Rayleigh wave, which has bad simulation. This requires a big negative *S* velocity correction in the lithosphere layers and small negative corrections in mantle layers down to the 630*km* depth. Further observation on these two repetitive depth phases of *ScS* and ScS_2 waves, the synthetic from the *PREMAN* arrives also a little earlier. The minima location of the wave was observed. To overcome the problem, the correction on the *S* velocity structure is required. Correction on β_v is imposed on the earth layers, from the earth crust down to the base mantle layers using small negative values on zero order coefficients of polynomial of the *S* velocity function in these layers. It is surprised that the correction of β_h in the base mantle layer does not bring the improvement in *ScSH*. In contrary, the change in the β_v velocity has a big influence on *ScSH*. The distinct discrepancies on the *SH* and *SV* wave show that the corrected values for the β_v and β_h are different, from the lithosphere

layers to 630*km* depth. It shows that vertical anisotropy is also occurred in earth layers down to 630*km* depth.

Next is the seismogram analysis of *C051194C* earthquake at *CHTO* and *ENH* observation stations as illustrated in Figures (6) and (7). The epicentral distance of *ENH* station to *C051194C* hypocenter is 33.8°, so the *ScS* is immersed in the Love waveform, and therefore, it can not be seen. The strong negative anomaly in the upper mantle is also shown by the seismogram fitting at these stations.

Figure (8) presents a seismogram analysis and matching of *C010498A* earthquake in the *QIZ* station, ranging from the *S* wave phase to the Love and Rayleigh surface waves, and core reflected *ScS* wave. We notice the fitting of this seismogram in the *QIZ* station, as being pointed out in the Figure (8a). Fitting is obtained on the beginning of the Love wave, by giving small negative correction on the β_h and changing of the β_h gradient in the upper mantle layers. Evidently the correction of the *SH* velocity in the upper mantle is also required to achieve a good fitting, ranging from the *SS* wave to the *S* wave. A good fitting is also obtained for the Rayleigh wave, where big negative correction is imposed on *SV* in the lithosphere layers. The small *S* wave correction is imposed in the mantle layers in order to get the fitting for the *S* wave in the three Cartesian components. Figure (8b) presents seismogram fitting of the *C010498A* earthquake in the *QIZ* station for the *ScS* wave. By imposing the small correction in the *SV* velocity in the base mantle layers, the fitting achieved is excellent for the *ScS* wave in the *r* component.
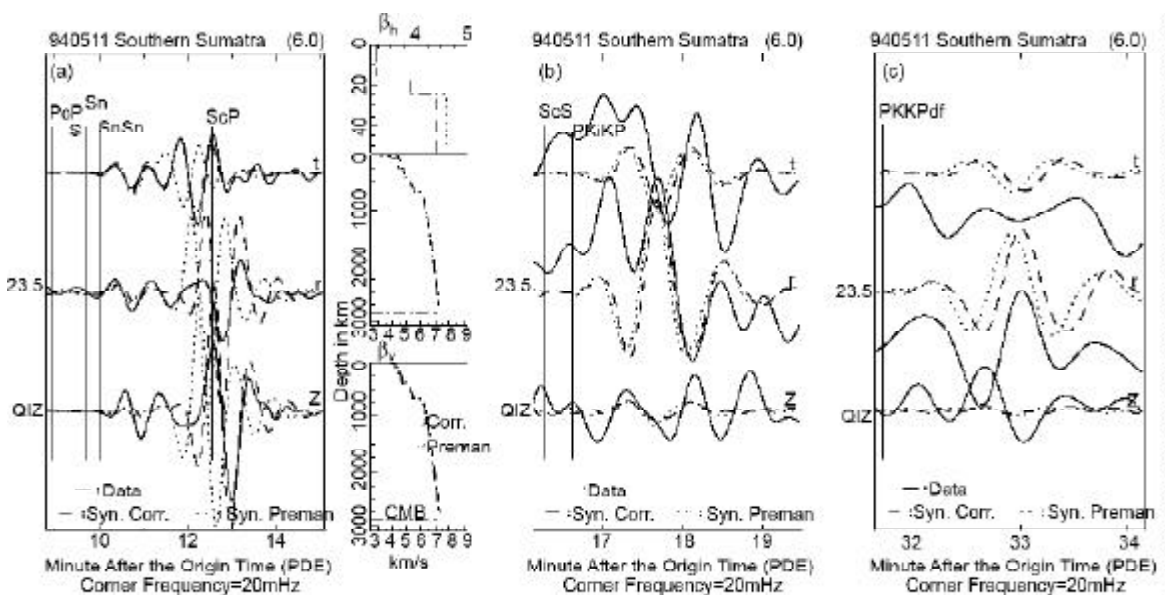

Figure 5. Seismogram analysis and fitting of C051194C earthquake in QIZ. waves: a) S-L-R; b) ScS; and c) ScS_2.
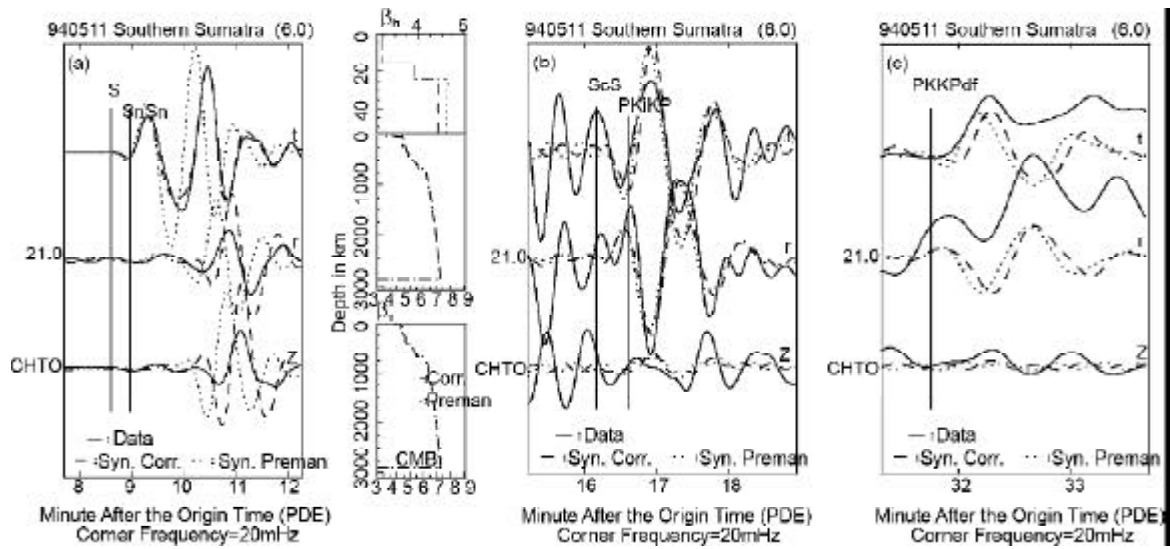
Figure 6. Seismogram analysis and fitting of C051194C earthquake in CHTO. waves: a) S-L-R; b) ScS; and c) ScS$_2$.
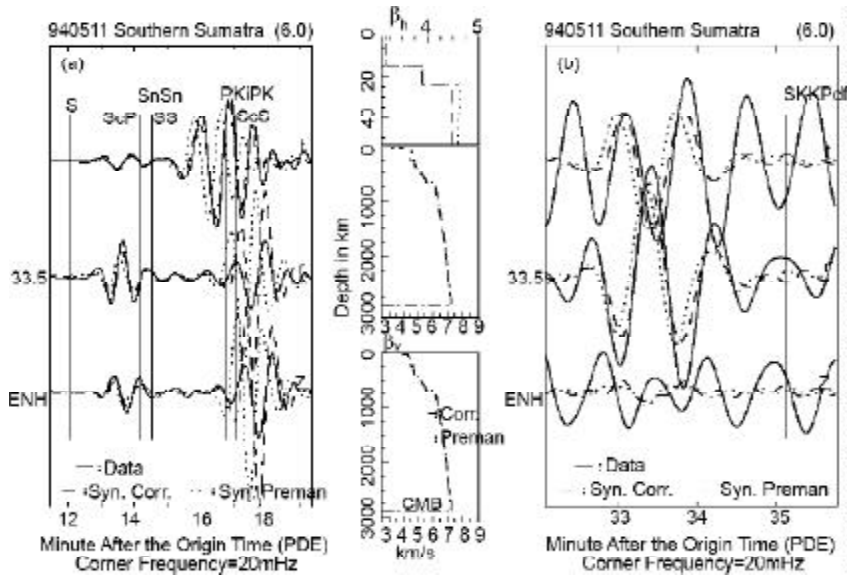

Figure 7. Seismogram analysis and fitting of C051194C earthquake in ENH. waves: a) S-L-R; and b) ScS.
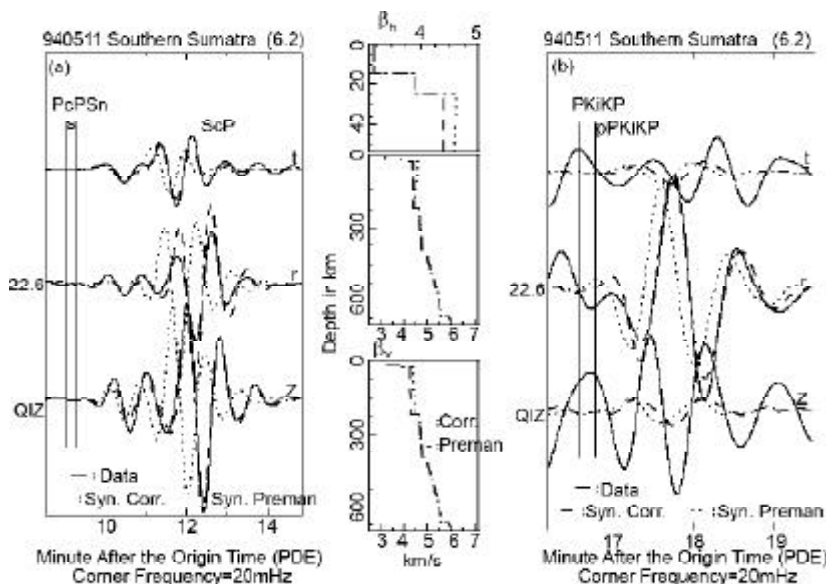

Figure 8. Seismogram analysis and fitting of C010498A earthquake in QIZ. waves: a) S-L-R; and b) ScS.

Figure (9) presents the analysis and fitting of the *C*080493*C* seismogram in the *QIZ* station, from the *S* wave phase to the Love and Rayleigh surface waves, and the right side figure is for the *ScS* wave. The positive gradient β_h and negative correction to *S* wave velocity are also imposed in the upper mantle layers. These efforts provide the fitting for Love wave. To achieve the fitting on the Rayleigh wave, big negative correction is also applied in the upper mantle layers. Further negative corrections are required on the layers below the upper mantle down to 630*km* depth, in order to achieve the fitting for the *S* and *ScS* waves and multiple *ScS*$_2$ and *ScS*$_3$.

Strong negative anomaly on *S* wave velocity in the upper mantle is also shown by the seismogram fitting in *ENH* and *SSE* observatory station. Although a weaker negative anomaly was also found in the layers below upper mantle down to *CMB*, which is shown by Figures (10) and (11).

Figure (12) presents the analysis and fitting of the *C*040198*A* seismogram in the *QIZ* station, from the *S* wave phase to the Love and Rayleigh surface waves, and the right side figure is for the *ScS* wave. The positive gradient β_h and negative correction to *S* wave velocity are also imposed in the upper mantle layers. Small velocity correction is imposed on zero order coefficients of β_h in the upper mantle layers, where these efforts provide the fitting for Love wave. To achieve the fitting on the Rayleigh wave, big negative correction is also applied in the upper mantle layers. Further negative corrections are required on the layers below the upper mantle down to *CMB*, in order to achieve the fitting for the *S* and *ScS* waves.
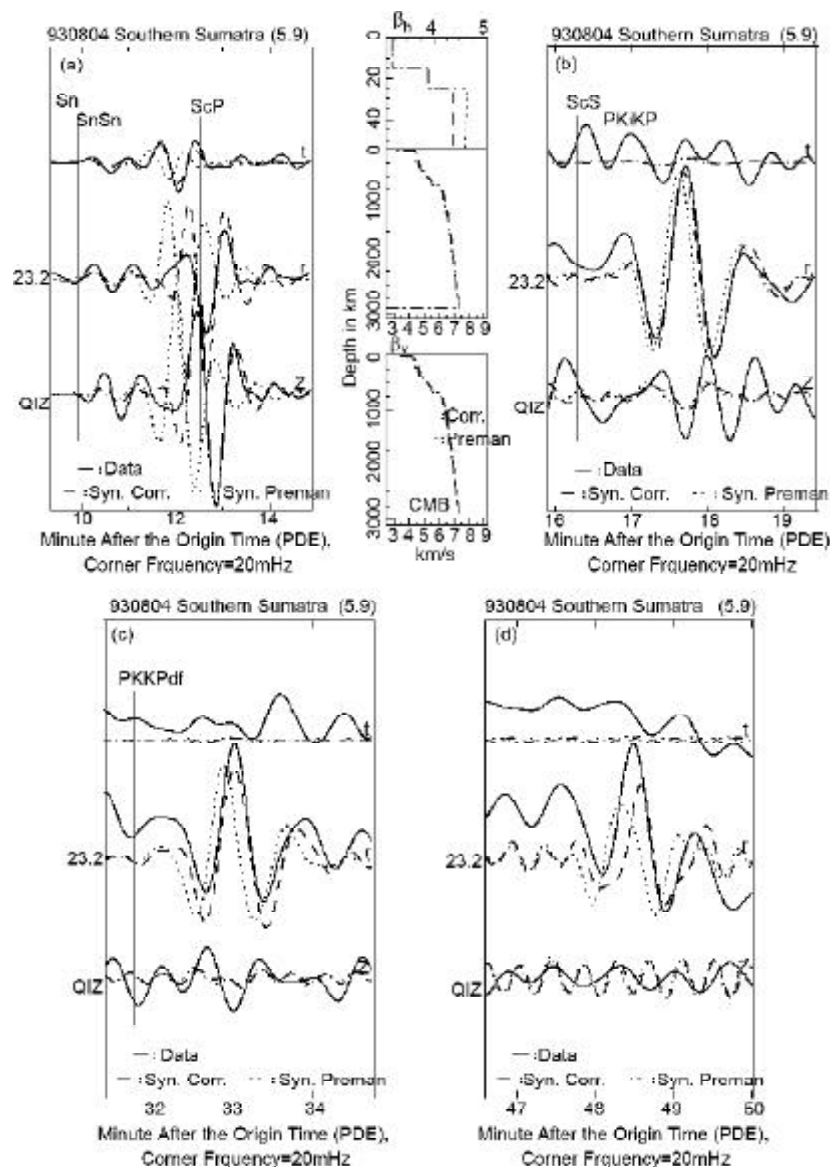

Figure 9. Seismogram analysis and fitting of C080493C earthquake in QIZ. waves: a) S-L-R; b) ScS; c) ScS$_2$; and d) ScS$_3$.
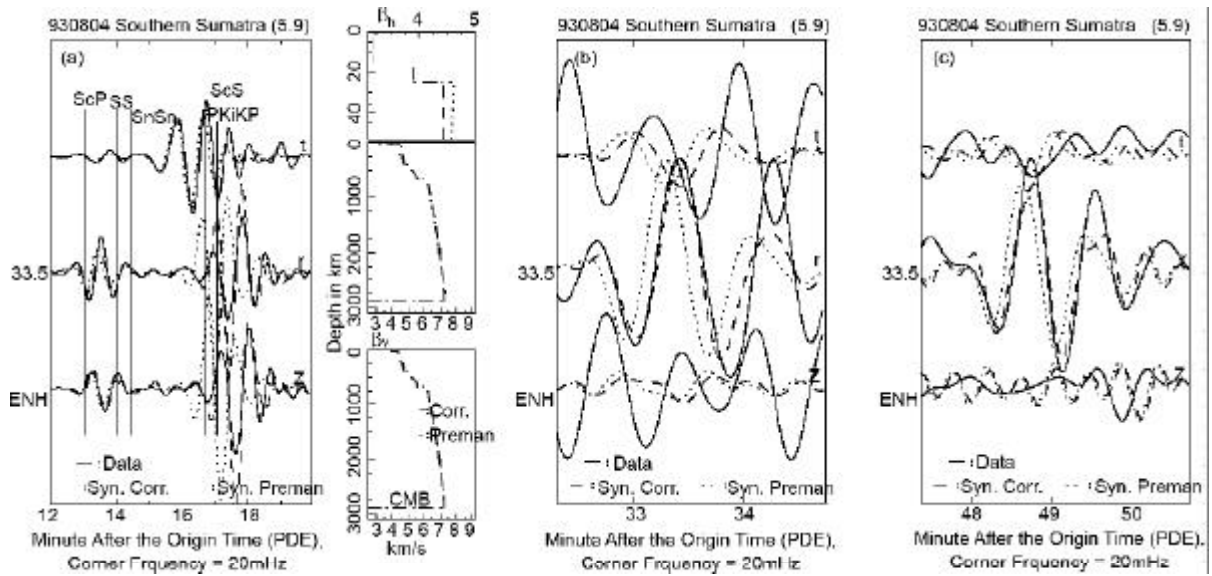
Figure 10. Seismogram analysis and fitting of C080493C earthquake in ENH. waves: a) S-L-R; b) ScS$_2$; and c) ScS$_3$.
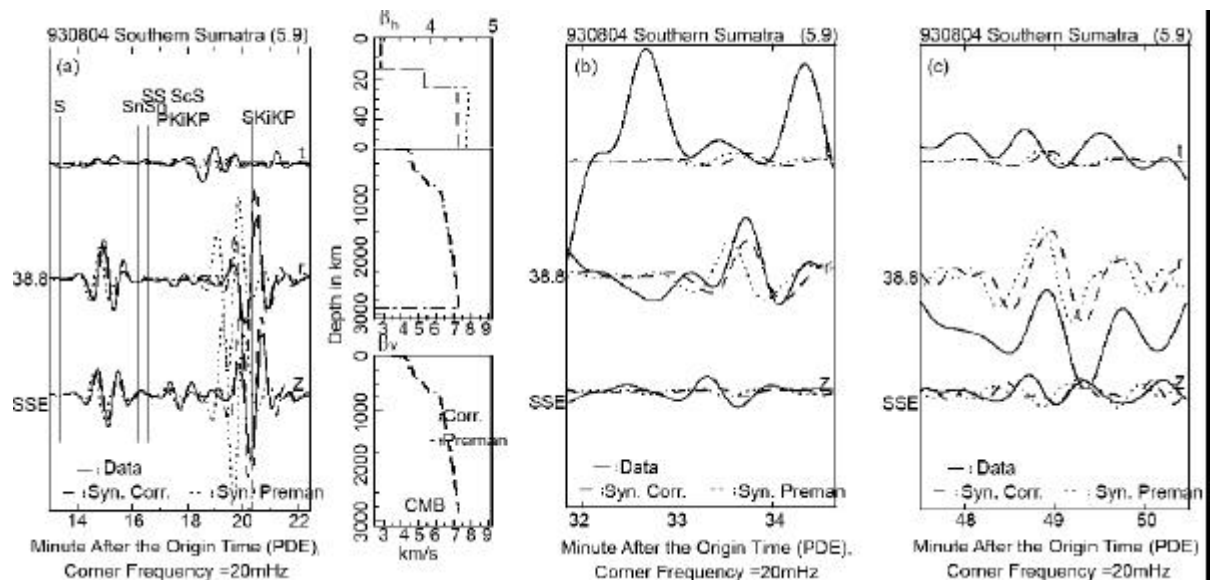

Figure 11. Seismogram analysis and fitting of C080493C earthquake in SSE. waves: a) S-L-R; b) ScS$_2$; and c) ScS$_3$.
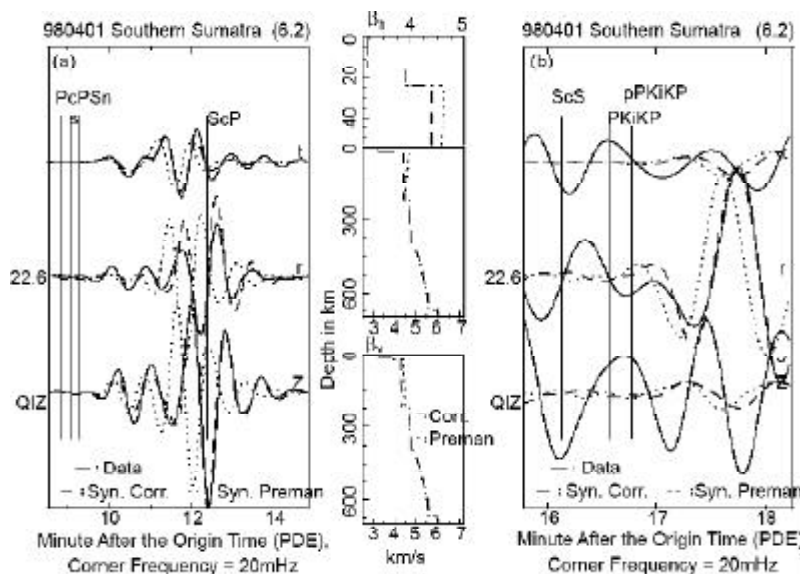

Figure 12. Seismogram analysis and fitting of C040198A earthquake in QIZ. waves: a) S-L-R; and b) ScS.

Figure (13) presents the seismogram fitting of *C*040198*A* earthquake in *CHTO* station for *S* wave to Love and Rayleigh surface wave, and multiple core reflected *ScS* and *ScS*$_2$. This shows that the negative corrections on zero order coefficients of β_v must be carried out in all mantle layers.

Figure (14) presents the analysis and fitting of the *C*040198*A* seismogram in the *KMI* station, from the *S* wave phase to the Love and Rayleigh surface waves, and the right side figure is for the *ScS*$_2$ wave. The positive gradient β_h and negative correction to *S* wave velocity are also imposed in the upper mantle layers. Small velocity correction is carried out on zero order coefficients of β_h in the upper mantle layers, where the fitting for *S* and Love wave is achieved.

To achieve the fitting on the Rayleigh wave, big negative correction is also applied in the upper mantle layers. Further negative corrections are required on the layers below the upper mantle down to *CMB*, in order to achieve the fitting for the *ScS*$_2$ waves.

4.2. Discussion

The seismogram processing of the earthquakes began from the *B*051194*F* and *C*051194*C* earthquakes, where is very close to each other, but has 13 hours time difference of their occurrence. The obtained earth model from the analysis on the *B*051194*F* earthquake has tried to reconstruct the synthetic seismogram of *C*051194*C* earthquake in the *QIZ* station. But evidently the result of the synthetic
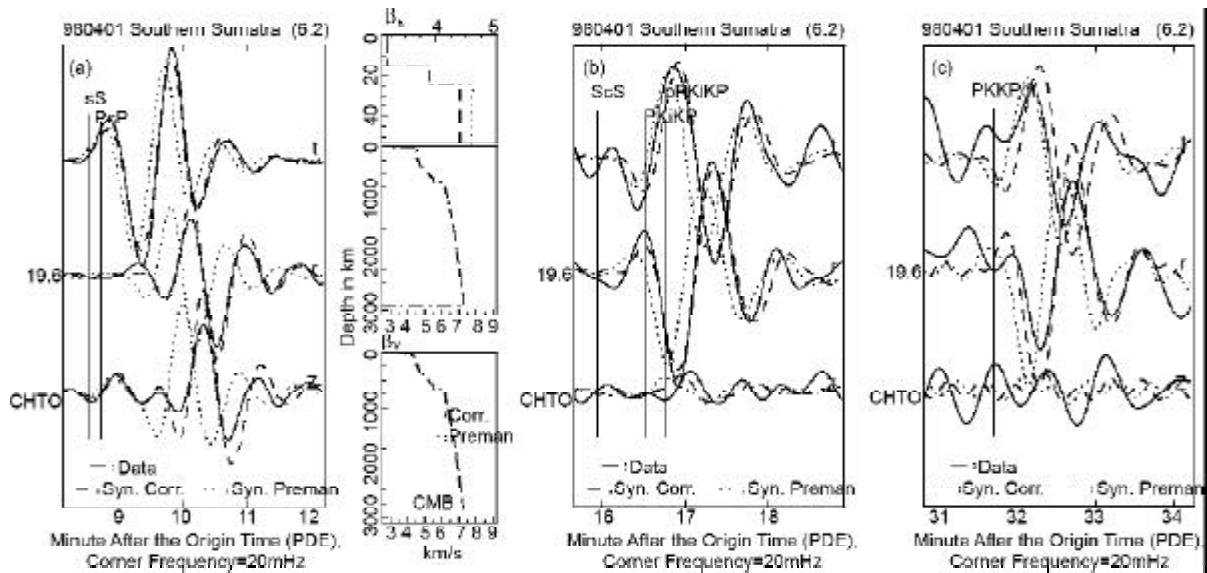

Figure 13. Seismogram analysis and fitting of C 040198A earthquake in CHTO. waves: a) S-L-R; b) ScS; and c) ScS$_2$.
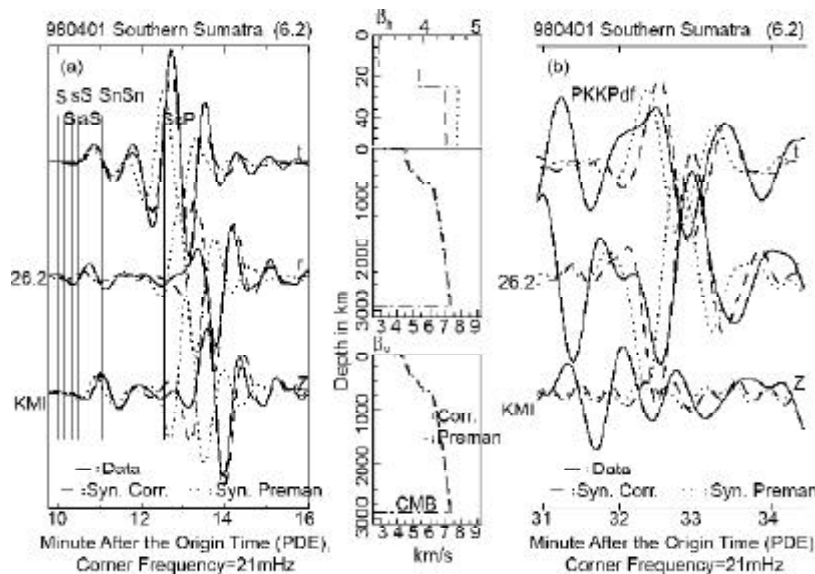

Figure 14. Seismogram analysis and fitting of C040198A earthquake in KMI. waves: a) S-L-R; and b) ScS$_2$.

seismogram from the *B*051194*F* earth model still has seismogram discrepancy to the Love wave. The synthetic Love wave must then be reconstructed for the corrected earth model. The obtained negative anomaly of *S* velocity structure is also to reconstruct the synthetic seismogram in *CHTO*, *KMI*, *ENH* and *SSE* stations. The synthetic seismogram approximate the appropriate observed seismogram, but still needs the fine corrections to achieve the waveform fitting for Rayleigh and Love waves. This indicates that the strong negative corrections must be imposed on upper mantle layers and small negative corrections for deeper earth mantle layers down to *CMB*. The hypocenter locations of the third and fourth analyzed earthquakes are also close to each other. Different efforts to get the seismogram fitting from these four earthquakes give indication, that the earth model is necessarily more heterogeneous than supposed by other seismologists, despite the seismogram analysis is only done in the frequency as low as 40*mHz*.

Attention should be also paid on the amplitude difference in Love and Rayleigh waves; the supposed homogeneous and isotropic earth model for the determination of the *CMT* solution of the earthquake. The maximum frequency used in this research is 40*mHz*, four times higher than the one used to calculate the Kernel function in the determination of the *CMT* solution [16].

Figures that contain the wave phase of *ScS* and *ScS$_2$*, see Figures (3) to (14), show that the fitting is achieved by altering the β_v in the base mantle layers. Meanwhile, the change of β_h does not bring significant repair on the deep wave fitting. According to Guo et al [15], in order to obtain the fitting on *ScSH*, the velocity structure of β_h near *CMB* should have strong sensitivity, as illustrated in Figure (15), while the results of this research show the contrary, that strong sensitivity on *ScS$_2$* wave comes from the β_v velocity structure near the *CMB*, see Figures of (3) to (14). These dependencies are not yet known by other seismologists. Another thing that has not also been known is that a vertical anisotropy occurs not only in the upper mantle layers, but also in earth layers from lithosphere down to *CMB*, as stated on the *PREMAN* earth model.

Table (2) shows the zero order coefficients of *SV* and *SH* velocities function from two stations, *CHTO* and *QIZ*. If we compare the values of *SV* and *SH* in radius from 3480*km* (Core Mantle Boundary, *CMB*) to 6291*km*, these two stations have different values for the same earth radius.

Table 2. Zero order coefficients of SV and SH wave velocity of CHTO and QIZ stations.

	CHTO			QIZ		
R	**SV**	**SH**	**R**	**SV**	**SH**
3480.0	6.9564	6.9254	3480.0	6.9414	6.9254
3630.0	11.1971	11.1671	3630.0	11.1821	11.1671
5600.0	22.3409	22.3409	5600.0	22.3409	22.3409
5701.0	9.9839	10.0429	5701.0	9.9829	10.0429
5771.0	22.3562	22.3992	5771.0	22.3362	22.3962
5971.0	8.9246	8.9896	5971.0	8.9246	8.9846
6151.0	5.7552	5.7632	6151.0	5.7352	5.8592
β_h Gradient	-1.4278				-1.4278
6291.0	5.7552	5.8392	6291.0	5.7352	5.8592
β_h Gradient	-1.4278				-1.4278
6346.0	3.9000	3.9000	6343.6	3.9000	3.9000
6356.1	3.2000	3.2000	6356.0	3.2000	3.2000

After changing the *S* velocity structure from the lithosphere down to *CMB*, the fitting is achieved on two wave phases, the surface wave and the *ScS* wave. The use of small epicentral distances stations to analyze the *ScS*, *ScS$_2$* and *ScS$_3$* wave phases has never been used until now by other seismologists. The other seismologist experts used the travel time using epicentral distances observatory stations over 83°, in order to get the time arrival differences of the wave phase of the *S-SKS*, *SKKS*, *SKIKS* [17-19], and to research the structure of the base mantle.

The wave paths from earthquake hypocenters to the *QIZ*, *CHTO*, *KMI*, *ENH*, and *SSE* observation stations pass across the earth structure in South-East Asia, where the analyzed area is in front area of the Indian subduction zone. The earth in the South-East Asian area evidently has the negative anomaly, from the lithosphere layers down to base mantle layers. This is required to obtain the fitting on the seismogram, from the surface wave to *S*, *ScS* and *ScS$_2$* body waves. Results of this research complete the results of the other seismological research in the same area that are merely based on the arrival time data and dispersion curves.
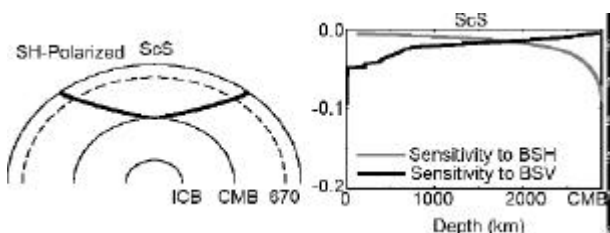

Figure 15. Sensitivity curve of ScSH arrival time against S velocity structure [15].

Castle et al [20] interpreted that the slow wave velocities show the hot thermal sign of slabs in the upper mantle. Slow wave velocities in the mantle layers are well correlated with hotspot locations. In their degree 30 model, slow regions correlate to the surface location of hotspots, supporting their previous observations. If no correlation existed between hotspot locations at the surface and slow anomalies in the lowermost mantle, it would strongly argue that hotspots do not originate within the basal layer. As indicated with the results of this research, is it true that the earth model beneath *SE* Asia is hotter?

5. Summary

This research analyzes the recorded seismogram at *CHTO*, Thailand, *QIZ*, *KMI*, *ENH* and *SSE* stations, China, where the ground movement is produced by four earthquakes in South Sumatra, Indonesia which lie close to each other. The comparison between the measured seismogram and the synthetic one, which is reconstructed from *PREMAN* earth model, shows that the synthetic seismogram deviates with earlier arrival time instead of measured arrival time. This result indicates that earth model ahead of Indian subduction zone has negative *S* wave velocity anomaly.

Correction of the *S* wave velocity structure is done first by noticing the fitting on the Love and Rayleigh surface wave, corrections cover the β_h positive gradient in the upper mantle layers, changes of earth crust thickness, for fitting at the Love waveform, and reduction of the zero order coefficient values at velocity polynomial function in the upper mantle layers for Rayleigh wave. The research result indicates that the upper mantle has negative anomaly for fitting at the Love and Rayleigh wave. The negative corrections continue to earth layers down to 630*km* depth. Further fitting on *ScS* and *ScS*$_2$ waves indicates that negative corrections also occur at the base mantle. The distinct correction values for β_h and β_v indicate that vertical anisotropy happened at all of earth mantle layers.

The result of the research shows that non-tectonic area in South-East Asia ahead of Indian subduction zone, has strong negative anomaly of *S* wave in the upper mantle layers and weak negativity below these layers until *CMB*. The *CMT* solution also shows mistakes if the surface wave amplitude of three components has different amplitude.

References

1. Hall, R. (2002). "Cenozoic Geological and Plate Tectonic Evolution of SE Asia and the SW Pacific: Computer Based Reconstructions, Model and Animations", *Journal Asian Earth Sciences*, **20**, 353-431.

2. Replumaz, A., Karason, H., Van Der Hilst, R.D., Besse, J., and Tapponnier, P. (2004). "4-D Evolution of SE Asia's Mantle from Geological Reconstructions and Seismic Tomography", *Earth and Planetary Science Letters*, **221**, 103-115.

3. Grand, S., Van Der Hilst, R., and Widiyantoro, S., (1997). "Global Seismic Tomography: A Snapshot of Convection in the Earth", GSA Today, **7**, 1-7.

4. Van Der Hilst, R., Widiyantoro, S., and Engdahl, E. (1997). "Evidence for Deep Mantle Circulation from Global Tomography", Nature, **386**, 578-584.

5. Bijwaard, H., Spakman, W., and Engdahl, E. (1998). "Closing the Gap Between Regional and Global Travel Time Tomography", *Journal of Geophysical Research*, **103**, 30055-30078.

6. Boschi, L. and Dziewonski, A. (1999). "High- and Low-Resolution Images of the Earth's Mantle: Implications of Different Approaches to Tomographic Modeling", *Journal of Geophysical Research*, **104**, 25567-25594.

7. Zhou, H. (1996). "A High-Resolution P Wave Model for the Top 1200km of the Mantle", *Journal of Geophysical Research*, **101**, 27791-27810.

8. Zhao, D. (2001). "Seismic Structure and Origin of Hotspots and Mantle Plumes", *Earth and Planetary Science Letters*, **192**, 251-265.

9. Dalkolmo, J. (1993). "Synthetische Seismogramme Fuer Eine Sphaerisch Symmetrische, Nichtrotierend Erde Durch Direkte Berechnung der Greenschen Funktion", Diplomarbeit, Institut fuer Geophysik,

Universitaet Stuttgart.

10. Friederich, W. and Dalkolmo, J. (1995). "Complete Synthetic Seismograms for a Spherically Symmetric Earth by a Numerical Computation of the Green's Function in the Frequency Domain", *Geophysical Journal International*, **122**, 537-550.

11. Bulland, R. and Chapman, C. (1983). "Travel Time Calculation", Bulletin of Seismological Society of America, **73**, 1271-1302.

12. Dziewonski, A.M. and Anderson, D.L. (1981). "Preliminary Reference Earth Model", Physics of the Earth and Planetary Interior, **25**, 297-356.

13. Kennett, B.L.N. (1991). "Seismological Tables, Research School of Earth Sciences", Australian National University, IASPEI.

14. Kennett, B.L.N. Engdahl, E.R., and Buland R. (1995). "Constraints on Seismic Velocities in the Earth from Travel Times", *Geophysical Journal International*, **122**, 108-124.

15. Guo,Y.J., Lerner-Lam, A.L., Dziewonski, A.M. and Ekstram, G. (2005). "Deep Structure and Seismic Anisotropy Beneath the East Pacific Rise", Earth and Planetary Science Letters, **232**, 259-272.

16. Dreger, D.S. (2002). "Time-Domain Moment Tensor INVerse Code (TDMT_INVC)", The Berkeley Seismological Laboratory (BSL), Report Number 8511.

17. Wysession, M., Lay, T., and Revenaugh, J. (1998). The D" Discontinuity and Its Implications", In: Gurnis, M., Buffett, B., Knittle, K., and Wysession, M. (Eds.), The Core-Mantle Boundary, AGU, 273-297.

18. Boschi, L. and Dziewonski, A.M. (2000). "Whole Earth Tomography from Delay Times of P, PcP, and PKP Phases: Lateral Heterogeneities in the Outer Core or Radial Anisotropy in the Mantle?", *Journal of Geophysical Research*, **105**, 13675-13696.

19. Souriau, A. and Poupinet, G. (1991). "A Study of the Outermost Liquid Core Using Differential Travel Times of the SKS, SKKS and S3KS Phases", Physics of the Earth and Planetary Interior, **68**, 183-199.

20. Castle, J.C., Creager, K.C., Winchester, J.P., and R.D. Van Der Hilst (2000). "Shear Wave Speeds at the Base of the Mantle, *Journal of Geophysical Research*, **105**(B9), **21**, 543-557.